



# Fabrication of Highly Flat, Flexible Mesh Electrode for Use in Photovoltaics

Zhaoyang Zhong<sup>1</sup> · Pyeongsam Ko<sup>1,2</sup> · Hongseok Youn<sup>2</sup> · Areum Kim<sup>1</sup> · Kyoohee Woo<sup>1</sup>

Received: 18 October 2020 / Revised: 3 December 2020 / Accepted: 28 December 2020  
© Korean Society for Precision Engineering 2021

## Abstract

Metal mesh-based flexible transparent conductive electrodes have attracted much interest as one alternative to conventional indium tin oxide electrodes. In addition to ongoing efforts to develop scalable and cost-effective fabrication processes for high-resolution mesh patterns, the high surface roughness of the mesh which can cause short circuiting and current leakage in optoelectronic devices must be solved. Herein, high-resolution (below  $\sim 10\ \mu\text{m}$ ) mesh patterns with various thicknesses are fabricated by scalable, selective transfer printing and then stably and sufficiently sintered under delicately controlled flash irradiation. A polyethylene terephthalate (PET) film is laminated on the patterns overlaid with a UV-curable resin and then peeled off after UV curing, which produces mesh patterns strongly bonded to the cured resin to be separated in a fully embedded form. The final, highly flat, flexible mesh with a low sheet resistance of  $1.7\ \Omega\ \text{sq}^{-1}$ , a high optical transparency of 88.6%, excellent mechanical flexibility, and strong adhesion to the substrate is successfully implemented in a flexible perovskite solar cell with a high power conversion efficiency (PCE) of 14.92%.

**Keywords** Flat and flexible metal mesh electrode · Selective transfer printing · Flash lamp annealing · Perovskite solar cell

## 1 Introduction

Much effort has been made to implement new attractive features (e.g., flexibility, portability, and wearability) in optoelectronic devices such as photovoltaics [1–4], displays [5–7], and touch sensors [8–10] for some benefits such as conformability on uneven surface and easy transportation

and storage, as exemplified by the development of flexible transparent conductive electrodes (FTCEs) as an alternative to conventional indium tin oxide (ITO). Despite the good optoelectronic properties and reliability of ITO, its use in flexible electronics is hindered by the poor mechanical flexibility of the material [11–13]. Accordingly, various emerging FTCEs based on graphene, carbon nanotubes, conducting polymers, metal nanowires, and metal meshes have been explored as ITO replacements. Fundamental studies on the synthesis of these materials have resulted in the proposal of scalable and low-cost fabrication processes, and the usefulness of these materials has been proven by their adoption in practical electronic applications. Despite the remaining commercialization challenges, the above materials are expected to dominate the transparent conductive electrode market in the near future with the rise of flexible electronics [14–24].

Compared with other alternatives, metal mesh-based FTCEs offer remarkable advantages, as their transparency and sheet resistance can be precisely tuned in a wide range by varying mesh geometry, line width/spacing, and metal thickness. In particular, it is quite attractive that sufficiently high conductivity can be achieved without deteriorating transmittance by increasing the pattern height (thickness) while maintaining the opaque area covered

Zhaoyang Zhong and Pyeongsam Ko contributed equally to this work.

**Supplementary Information** The online version contains supplementary material available at <https://doi.org/10.1007/s40684-020-00308-1>.

✉ Areum Kim  
arkim@kimm.re.kr

✉ Kyoohee Woo  
khwoo@kimm.re.kr

<sup>1</sup> Nano-Convergence Manufacturing Systems Research Division, Korea Institute of Machinery and Materials (KIMM), Daejeon 305-343, Republic of Korea

<sup>2</sup> Department of Mechanical Engineering, Hanbat National University, Dongseodaero 125, Yuseong-gu, Daejeon 34158, Republic of Korea

by the mesh pattern [25]. Despite this advantage, several critical problems must be solved to enable the widespread use of mesh FTCEs. One such problem is high surface roughness, which can lead to short-circuiting or current leakage in optoelectronic devices comprising multiple thin layers [19]. As a solution, many researchers have tried to smooth the surface by applying an additional conductive overlayer (e.g., PEDOT:PSS) on top of the mesh. Even though this strategy can effectively lower surface roughness and thus prevent short-circuiting, it only works for thin metal meshes and sometimes causes transmittance loss [19–22]. Therefore, several approaches for embedding the mesh into the underlying substrate have been developed. For the embedded mesh, the method of filling pre-formed trenches on the substrate with metal nanoparticle (NP) ink has been widely used [26–30]. However, in this case, it is difficult to achieve a completely flat surface, as trenches cannot be entirely filled up with the metal because of unintended phenomena such as ink solvent evaporation and volume shrinkage due to NP sintering. Although additional electroless metal deposition or electroplating allow one to fill the underfilled trenches, this strategy increases processing time and cost [31–33]. Therefore, a cost-effective, large-scale method of fabricating fully filled, highly flat, fine meshes without additional processes should be developed to accelerate the commercialization of mesh FTCEs.

Herein, we suggest a new method of fabricating highly conductive and flat fine metal mesh-based FTCEs. Ag NP-based high-resolution (below  $\sim 10 \mu\text{m}$ ) mesh patterns with various thicknesses are produced on a glass substrate via a scalable and selective transfer printing process. Then, flash lamp annealing (FLA) is used to rapidly remove the residual insulating organics and sinter NPs in the as-printed patterns over a large area. The electrical properties and sintering behavior of patterns after irradiation with various flash sequences (e.g., single flash, dual flash, and multiple flashes) are investigated to show that well-sintered highly conductive meshes can be obtained without any detrimental faults such as pattern delamination. For the complete embedding of fine meshes, a UV-curable resin is laminated on the mesh patterns with a polyethylene terephthalate (PET) film and then photocured. The PET with cured resin is peeled off, and the mesh is separated together with the tightly bound resin. As a result, an impeccably flat and fine mesh FTCE is obtained, featuring a low sheet resistance ( $R_s$ ) of  $1.7 \Omega \text{ sq}^{-1}$ , an optical transparency of 88.6%, high mechanical flexibility, and strong adhesion to the substrate. This mesh FTCE is employed in the fabrication of a flexible perovskite solar cell (PSC) with a high power conversion efficiency (PCE) of 14.92%. This structure holds great promise for use in flexible optoelectronic devices.

## 2 Experimental

### 2.1 Fabrication of the Flat Mesh Electrode

Selective transfer printing was employed to prepare fine mesh patterns. First, Ag NP-based ink (DGH-RO, Advanced Nano Product Inc., Korea) was spin-coated on a PDMS-based coating blanket (Fujikura Composites, Japan). To control mesh pattern thickness, the spin-coating rate was tuned to 1000, 3000, and 7000 rpm with a fixed time of 60 s. Then, a metal cylinder wrapped with a different blanket (R16, KNW, Korea) was rolled over the coating blanket at a speed of  $6 \text{ mm s}^{-1}$  and a force of 10 kgf. Owing to the engineered surface energy of the roll blanket, which exceeded that of the coating blanket, the semidried ink film was transferred to the roll blanket. In the selective transfer process, the ink coated on the blanket roll was brought into direct contact with an imprinted cliché (Nanofab, Korea) having a surface energy higher than that of the roll blanket at a speed of  $4 \text{ mm s}^{-1}$  under a force of 13 kgf. In this step, the ink film coated on the roll blanket was partially transferred to the patterned cliché. Finally, the patterns remaining on the roll blanket were set onto a  $200 \text{ mm} \times 200 \text{ mm}$  soda lime glass (1.8 T, L.C.D. TEC., Korea) substrate at a moving speed of  $6 \text{ mm s}^{-1}$  and a printing force of 12 kgf. The printed patterns were annealed using a Xe lamp flash system (Novacentrix, USA) with a broadband wavelength output of 200–1500 nm. To embed mesh patterns, a UV-curable resin (MINS-311RM, Minuta Technology Co., Ltd., Korea) with a PET (SH71, SKC, Korea) film was laminated on patterns and then cured by UV light (Minuta Technology Co., Ltd., Korea) for 10 s. Finally, the PET film was peeled off with the cured resin, and the mesh electrode was delaminated while remaining buried in the resin.

### 2.2 PSC Fabrication

The PSC was fabricated as described elsewhere [44]. An AZO layer with a thickness of  $\sim 50 \text{ nm}$  ( $T\% = 93.3\%$  and  $R_s \approx 588 \Omega \text{ sq}^{-1}$ ) was deposited on the embedded fine-mesh FTCE by atomic layer deposition (NCD Inc., Daejeon, Korea) as a protective barrier to prevent the Ag mesh from being corroded by perovskite-derived halogen species. Then, an  $\text{SnO}_2$  ETL was spin-coated using a 1:1 (v/v) mixture of 3 wt%  $\text{SnO}_2$  colloid precursor (15 wt% colloidal dispersion in  $\text{H}_2\text{O}$ , Alfa Aesar, Ward Hill, MA, USA) and EDTA (99.995%, Sigma Aldrich) (16.7 wt% in deionized water) solutions and heated on a hot plate at  $60^\circ \text{C}$  for 30 min. For the triple-cation perovskite absorber layer, 223.56 mg of FA iodide (FAI,  $> 99\%$ ,

Greatcell Solar, Queanbeyan, Australia), 653.25 mg of  $\text{PbI}_2$  (99.995%, Alfa Aesar), 29.1 mg of methylammonium bromide (MABr, > 99%, Greatcell Solar), and 104.1 mg of  $\text{PbBr}_2$  (99.999%, Sigma-Aldrich) were dissolved in a mixture of 0.9 mL of dimethylformamide (DMF; 99.8%, Sigma-Aldrich) and 0.1 mL of dimethyl sulfoxide (DMSO; 99.9%, Sigma-Aldrich). This solution was then supplemented with a CsI solution (0.4  $\mu\text{L}$ ) prepared by dissolving 506.63 mg of CsI (99.999%, Sigma-Aldrich) in 1 mL of DMSO. The prepared solution was spin-coated in two steps of 1200 rpm/12 s and 6000 rpm/20 s, which was followed by annealing at 100 °C for 60 min in air. The solution for HTL deposition was formulated by mixing spiro-OMeTAD (99%, Sigma-Aldrich) and poly(3-hexylthiophene-2,5-diyl) (P3HT, Alfa Aesar) solutions in a volume ratio of 92:8. The spiro-OMeTAD solution was prepared by dissolving 72 mg of spiro-OMeTAD in a solution containing 1 mL of chlorobenzene, 28.8  $\mu\text{L}$  of 4-tert-butylpyridine (TBP; 98%, Sigma-Aldrich), and 17.5  $\mu\text{L}$  of a lithium salt solution prepared by dissolving 520 mg of bis(trifluoromethane)sulfonimide lithium salt (Li-TFSI, 99.95%, Sigma-Aldrich) in 1 mL of acetonitrile. The P3HT solution was prepared by mixing a solution of 15 mg of P3HT in 1 mL of chlorobenzene with 20.4  $\mu\text{L}$  of the Li-TFSI solution and 28.8  $\mu\text{L}$  of TBP. The Li-TFSI solution was prepared by dissolving 28.3 mg of Li-TFSI in 1 mL of acetonitrile. The HTL precursor solution was spin-coated on the perovskite layer at 3000 rpm for 30 s. Finally, an 80-nm-thick Au top electrode was deposited on the HTM layer by thermal evaporation.

### 2.3 Characterization of Mesh Electrodes and PSCs

Mesh pattern microstructures were observed by confocal OM (Optelics C130, Lasertec, Japan) and high-resolution FESEM (S4800, Hitachi Ltd., Japan). The  $R_s$  and  $T\%$  of mesh patterns were measured using a noncontact eddy-current probe system (EC-80-P, Napson Corp., Japan) and a UV-vis spectrophotometer (Lambda 750S, PerkinElmer, USA), respectively. Mechanical flexibility was evaluated using a custom-built automatic bending tester (iPen Co., Ltd., Korea). PSC performance was evaluated under the condition of 1.5 AM and 1 sun (100  $\text{mW cm}^{-2}$ ) using a solar simulator (Sol3A Class AAA, Oriel Instruments, Stratford, CT, USA) calibrated with a certified Si reference cell (Newport Corporation, Irvine, USA) and a Keithley 2400 source measurement unit (Keithley Instruments Inc., Cleveland, OH, USA). The active area (0.06  $\text{cm}^2$ ) of the PSC covered by an aperture mask was exposed to light. For statistical analysis, the current was obtained by scanning over a range of  $-0.1$  to  $1.2$  V at a rate of  $0.52$  V  $\text{s}^{-1}$  with a dwell time of 50 ms at each point.

## 3 Results and Discussion

High-resolution mesh patterns were fabricated by selective transfer printing (Fig. 1a and Fig. S1). Ag NP ink was spin-coated on a poly(dimethylsiloxane) (PDMS)-based coating blanket. In this step, the coating thickness could be varied by controlling the spin speed to afford final mesh patterns with desired thicknesses. During spin-coating, most of the solvent in the Ag NP ink was evaporated to form a semi-dried Ag NP ink film. Then, a metal cylinder wrapped by a roll blanket with a surface energy higher than that of the coating blanket was rolled over the semi-dried ink film to transfer it to the roll blanket. The ink film on the roll blanket was brought into contact with an intaglio-patterned cliché, and the unnecessary part of the ink film was transferred to the cliché convex patterns. In the final step, the remaining Ag NP patterns were transferred to the target substrate by rolling over a blanket-rapped cylinder. This printing process allowed the fabrication of fine mesh patterns with line widths below  $\sim 10$   $\mu\text{m}$  and thicknesses of 230–700 nm (Fig. 1b). Regardless of thicknesses, similar transmittance ( $T\%$ ) of  $\sim 88.5\%$  was observed (Fig. S2).

The Ag NP ink used for selective transfer printing has a high content of insulating organic additives including surfactants, tackifiers, and dispersants. Therefore, one should anneal the as-printed mesh patterns to decompose their additives along with sintering of NPs and thus increase conductivity [17]. This goal was achieved using an FLA method suited for fast and large-area processing. As shown in Fig. 2 and Table 1, 700 nm thick printed patterns were irradiated by various flash lights with controlled parameters (flash energy/power, irradiation time, and flash repetition number) and the electrical and morphological properties of the obtained samples were evaluated. In the case of single-flash irradiation, despite a constant total energy (9.17 J  $\text{cm}^{-2}$ ), the flash operated with higher power (higher voltage) and a shorter irradiation time (blue solid line in Fig. 2a) allowed the pattern to be instantaneously heated to higher temperature, inducing a significant reduction in  $R_s$  to  $3.8 \Omega \text{sq}^{-1}$  in less than a millisecond. However, at flash light powers above  $8.9 \text{ kW cm}^{-2}$ , the pattern was delaminated from the substrate (inset images in Fig. 2a), which was ascribed to a sudden large volume shrinkage due to the explosive decomposition of organic additives and the simultaneous sintering of Ag NPs.

A two-step irradiation sequence was used to further improve pattern conductivity without inducing delamination. The first flash was conducted at a power level below the detrimental delamination threshold to pre-anneal the pattern, while a second higher-power flash facilitated the decomposition of residual organics remaining after the

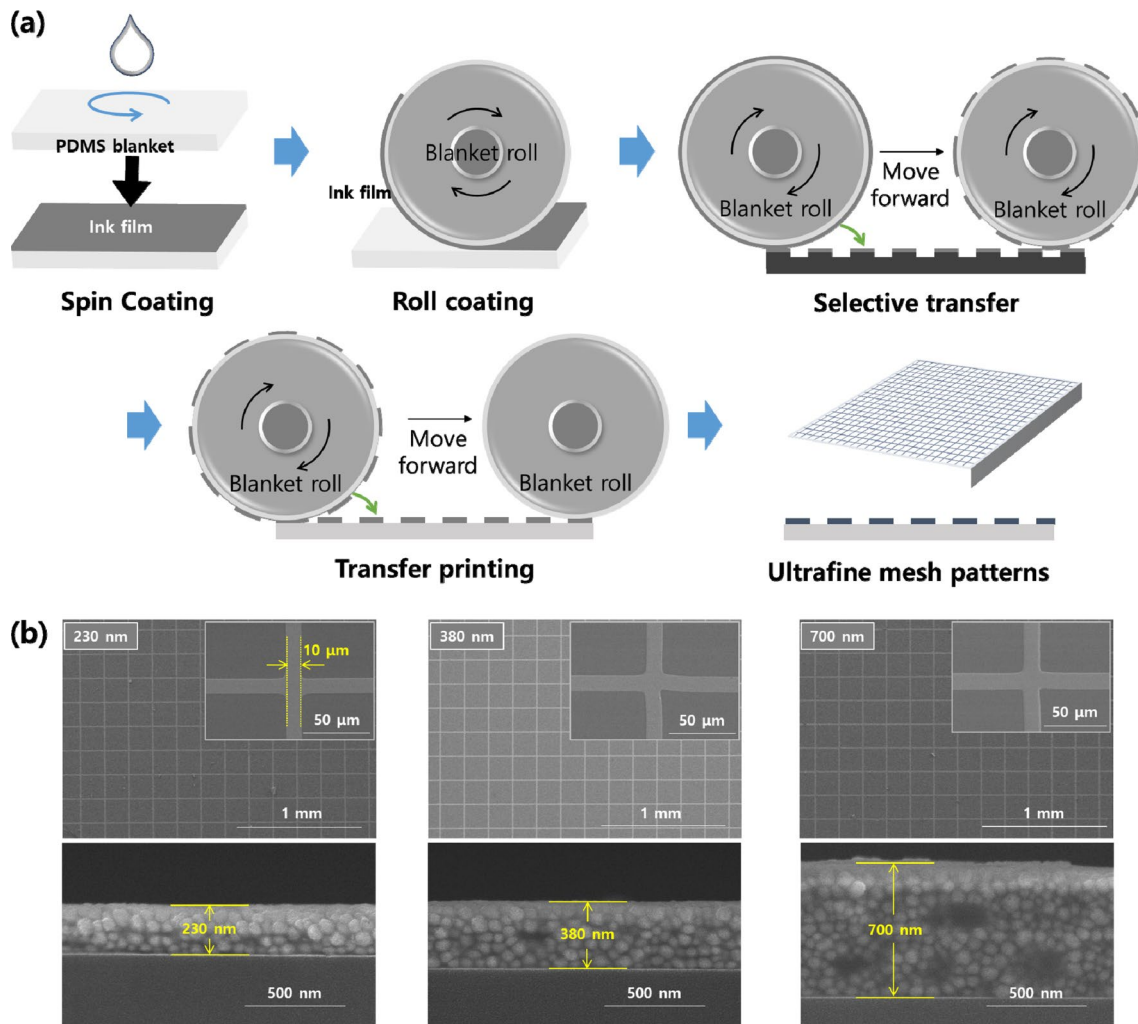


**Fig. 1** **a** Schematics of the selective transfer printing process, **b** FESEM images showing the plane and cross-sectional views of mesh patterns printed with thicknesses of 230, 380, and 700 nm

first flash and more efficiently sintering NPs. Specifically, the first flash was operated at a fixed condition of  $6.6 \text{ kW cm}^{-2}$  for 1700  $\mu\text{s}$ , which corresponded to the optimal condition of the single-flash method. The irradiation condition of the second flash was optimized by varying pulse power and energy, as shown in Fig. 2b and Table 1. The second flash was operated at a power of  $10.0 \text{ kW cm}^{-2}$  for 1200  $\mu\text{s}$  to afford a lower  $R_s$  of  $2.3 \Omega \text{ sq}^{-1}$ . Although the power of the second flash exceeded the single-flash delamination threshold of  $8.9 \text{ kW cm}^{-2}$ , no pattern damage was observed, as most of the organic additives had already been decomposed and the NPs had been sintered to some extent during pre-annealing by the first flash. Although the pattern was finally delaminated when the power of the second flash exceeded  $11.0 \text{ kW cm}^{-2}$ , stepwise annealing with two flashes was more suitable for stable annealing and higher conductivity than single-flash irradiation.

A logical extension of the two-flash strategy is the use of multiple flashes for more stable and sufficient heating. This strategy enables a repetitive and stable supply of heat for the steady and gradual decomposition of organics and NP sintering. The effectiveness of multiple-flash annealing was characterized by monitoring the effect of flash number on  $R_s$  (Fig. 2c and Table 1). For this experiment, we used a flash light with a power of  $6.6 \text{ kW cm}^{-2}$  that was proven not to damage the pattern, and light pulses were repeated at a fixed frequency of 1 Hz. The  $R_s$  of the mesh decreased with the increasing pulse number, reaching  $1.67 \Omega \text{ sq}^{-1}$  after 120 pulses. This value was close to that ( $1.68 \Omega \text{ sq}^{-1}$ ) achieved by conventional oven-annealing at  $350^\circ\text{C}$  for 30 min (Fig. S3), indicating that the mesh was fully sintered. As shown in Fig. S4a, the grain size increased because of significant NP sintering. Although the multiple-flash treatment increased the total time and



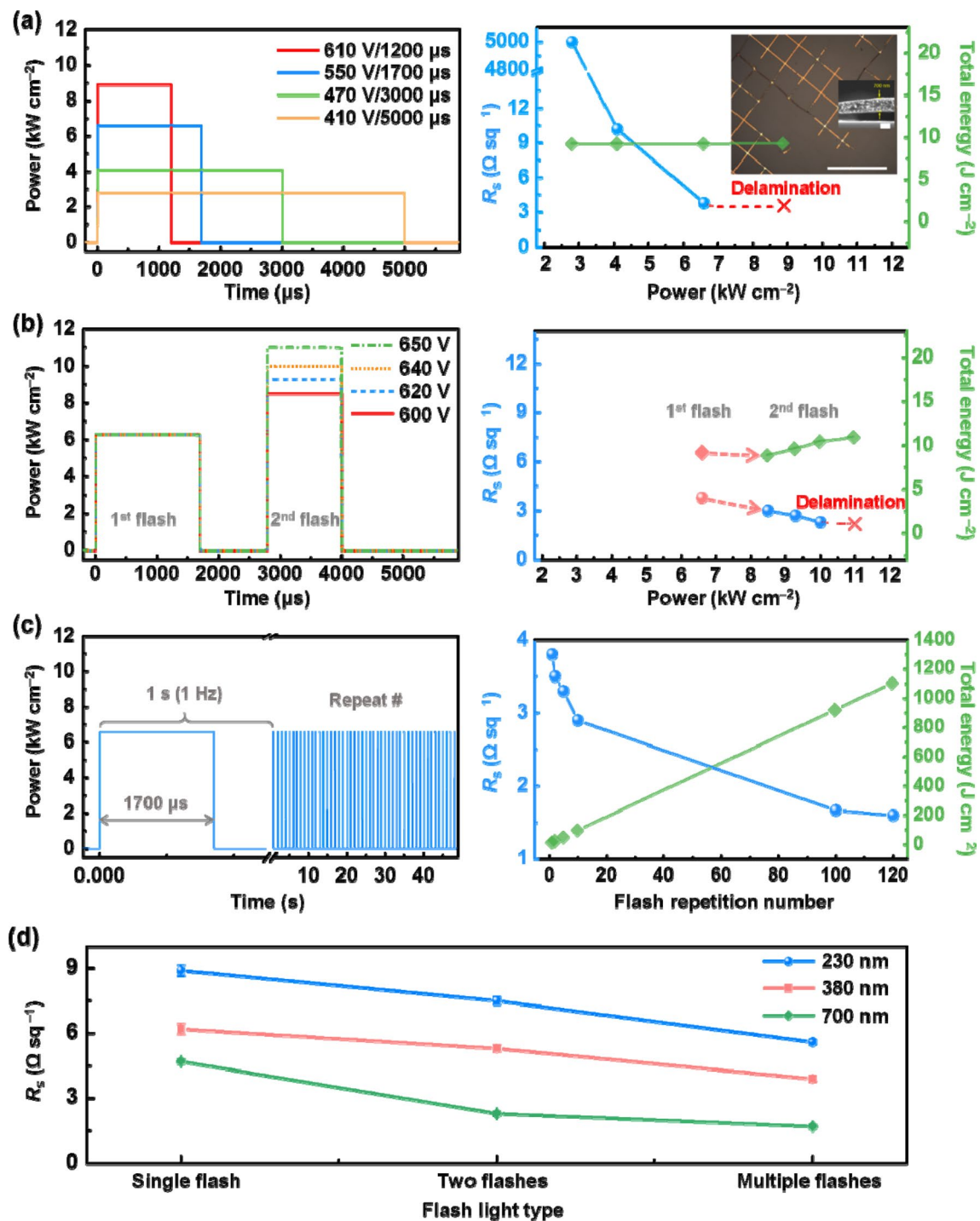


**Fig. 2** Operation conditions for **a** single-flash, **b** stepwise double-flash, and **c** multiple-flash irradiation, and the plot for the resultant sheet resistance of patterns and the total energy corresponding to each operating condition. In multiple flash irradiation, the number of flash

repetitions was varied from 1 to 120. **d** Best sheet resistances of mesh patterns with various thicknesses obtained after annealing by flash light treatments

energy required for processing, it was advantageous to the development of a sufficiently sintered, highly conductive pattern without sudden and large volume shrinkage.

For mesh patterns with thicknesses of 230 and 380 nm, the effects of irradiation mode on electrical properties and microstructures were investigated in the same manner with the overall results summarized in Fig. 2d, Table 2, and Fig.

**Table 1** Effects of flash light irradiation conditions on the  $R_s$  values of patterns

	Power [kW cm <sup>-2</sup> ] 1st pulse	Duration [μs]	Energy [J cm <sup>-2</sup> ]	Power [kW cm <sup>-2</sup> ] 2nd pulse	Duration [μs]	Energy [J cm <sup>-2</sup> ]	$R_s$ [Ω sq <sup>-1</sup> ]
Single flash	2.8	5000	9.17	—	—	—	> 5000
	4.1	3000	9.17	—	—	—	10.2 ± 0.148
	6.6	1700	9.17	—	—	—	3.8 ± 0.052
	8.9	1200	9.17	—	—	—	Delamination
Two flashes	6.6	1700	9.17	8.5	1200	8.78	3.0 ± 0.044
	6.6	1700	9.17	9.3	1200	9.55	2.7 ± 0.041
	6.6	1700	9.17	10.0	1200	10.38	2.3 ± 0.018
	6.6	1700	9.17	11.0	1200	10.87	Delamination
Multiple flashes	6.6	1700	9.17	1	9.17		3.8 ± 0.050
	6.6	1700	9.17	5	45.85		3.3 ± 0.048
	6.6	1700	9.17	10	91.7		2.9 ± 0.037
	6.6	1700	9.17	100	917.0		1.7 ± 0.029

**Table 2** Best  $R_s$  values of mesh electrodes with different thicknesses after various flash light treatments

Thickness [nm]	$R_s$ [Ω sq <sup>-1</sup> ]		
	Single flash	Stepwise two flashes	Continuous multiple flashes
700	3.8 ± 0.041	2.3 ± 0.032	1.7 ± 0.028
380	6.2 ± 0.054	5.3 ± 0.048	3.9 ± 0.040
230	8.9 ± 0.104	7.5 ± 0.087	5.6 ± 0.044

S4. For all samples, similar trends were observed in the electrical properties and sintering behaviors as a function of flash irradiation type. Irradiation with a single high-power flash in a short time could be suitable for high-speed NP pattern annealing. However, sufficient annealing of the printed pattern may be complicated by its easy delamination due to the sudden and instantaneous decomposition of organics and NP sintering at an overly high flash power. In this case, instead of a single flash, two or multiple flashes can be used to induce stepwise or gradual annealing and obtain a fully sintered, highly conductive pattern without delamination.

The printed and flash-annealed Ag mesh had an embossed surface, associated with its thickness, which was not suitable for optoelectronic devices. Therefore, we attempted to fabricate a highly flat FTCE by embedding the entire Ag mesh into a UV-curable resin. As illustrated in Fig. 3, the UV-curable resin was coated on the mesh pattern with a PET film, cured by UV light, and tightly coupled to the mesh pattern. Finally, the mesh-containing resin was peeled off from the glass substrate to afford a highly flat mesh FTCE.

Figure 4a shows optical microscopy (OM) and cross-sectional FESEM images of mesh patterns before and after embedding. OM images indicate that the fine mesh patterns could be transferred and embedded without any broken lines or fragments. In addition, the surface of the mesh FTCE was entirely flat without any bumps or trenches, as shown in the cross-sectional FESEM images and the inserted surface profiles.

To confirm the uniformity of this flat mesh FTCE, we probed its  $R_s$  distribution (Fig. 4b). The average  $R_s$  was determined as 1.67 Ω sq<sup>-1</sup> from the values measured at nine different regions within a 100 mm<sup>2</sup> area, and its deviation of 0.034 Ω sq<sup>-1</sup> indicated that the electrical properties of the FTCE in the tested area were fairly uniform. In addition, the intact transfer of Ag mesh patterns from the sacrificial glass to the resin/PET substrate as well as the related embedding were confirmed by the observation of small changes (~0.029 Ω sq<sup>-1</sup>) in average  $R_s$  before and after embedding. Moreover, embedding did not result in notable transparency degradation, as shown in Fig. 4b, c. The visible-light transmittance values of Ag mesh patterns prepared on glass and embedded in the polymer substrate were almost the same (88.6%).

The FTCE with an embedded Ag mesh had a highly flat surface with a low sheet resistance of 1.7 Ω sq<sup>-1</sup> and an optical transparency of 88.6% (at 550 nm). To enable comparison with previously reported results, we used the figure of merit (FoM) proposed by Dressel and Gruner [25], which is the ratio between direct current conductivity and optical conductivity at a wavelength of 550 nm. The FoM ( $\sigma_{dc}/\sigma_{opt}$ ) could be expressed as

$$\sigma_{dc}/\sigma_{opt} = 188.5/[R_s(T^{-1/2} - 1)],$$

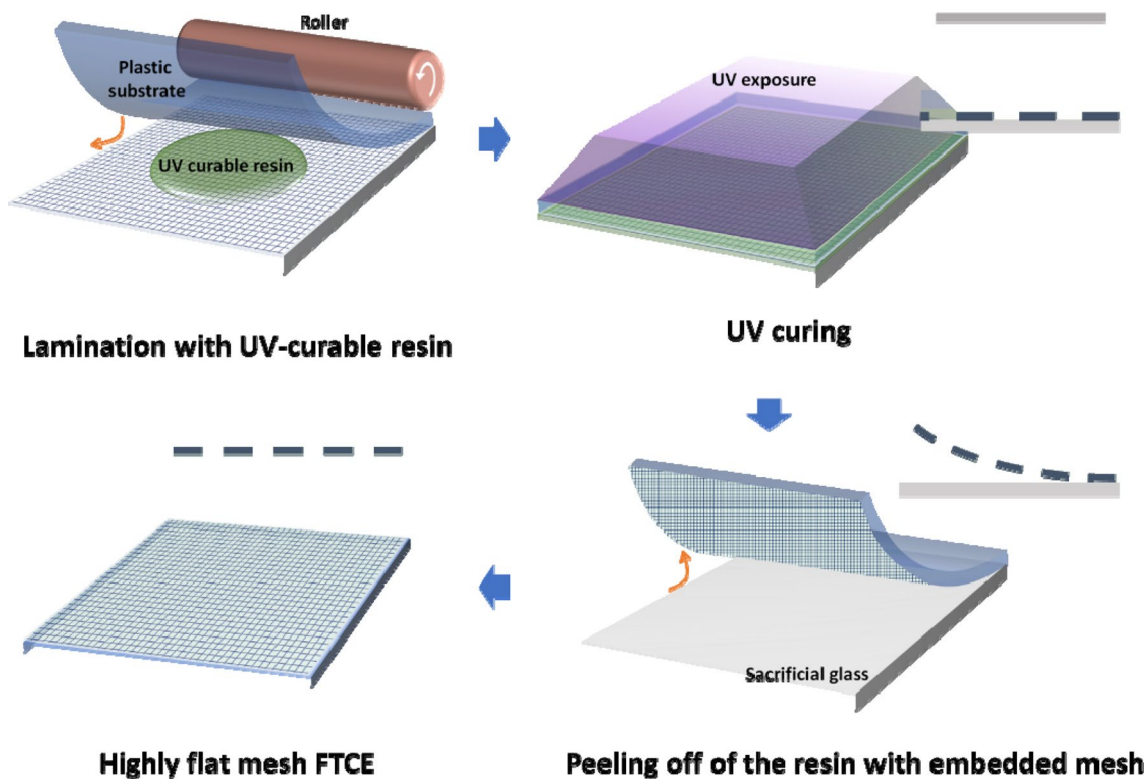
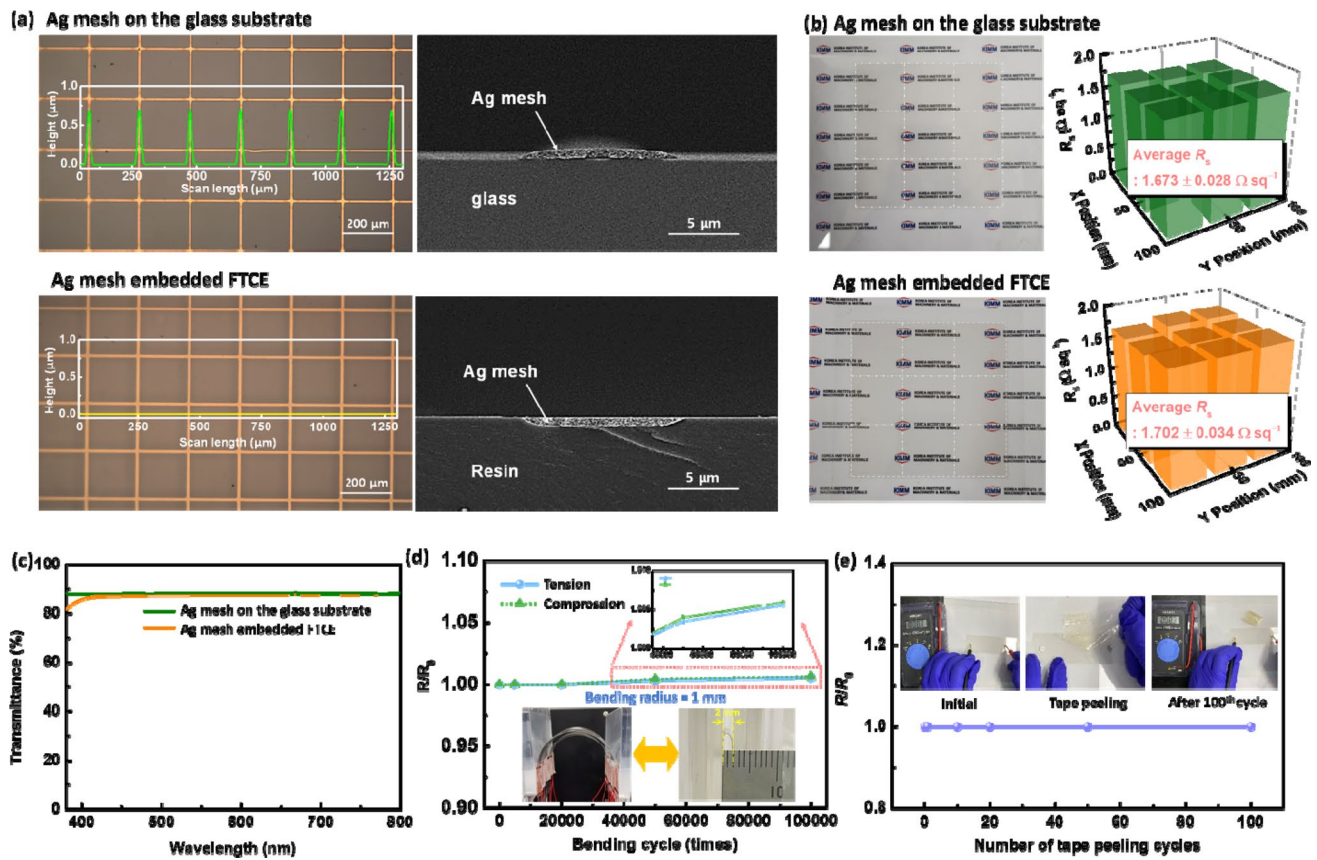


Fig. 3 Schematics of mesh pattern impregnation

where  $\sigma_{opt}$  is the optical conductivity at 550 nm, and  $\sigma_{dc}$  is the DC conductivity of the film. The calculated FoM ( $\sigma_{dc}/\sigma_{opt}$ ) and other characteristics (pattern line width, mesh thickness,  $T\%$  at 550 nm,  $R_s$ ) are summarized and compared in Table 3 and Fig. S5. It should be noted that these comparisons were limited to a Ag mesh based TCE with a flat surface. The FoM of our flat FTCE has a value of 1,777 which is quite competitive with similar structures that have been reported in the literature. The embedding of Ag mesh patterns into a polymer substrate also resulted in excellent flexibility and strong adhesion. Only a small increase in resistance was observed after 20,000 bending cycles at a curvature radius of 1 mm (Fig. 4d). In addition, adhesion properties were evaluated by monitoring changes in resistivity during repeated tape testing, and the resistivity of our FTCE was shown to stay nearly constant, even after the 100-fold attachment/detachment of a sticky tape (Fig. 4e).

To demonstrate the practical use of the fully embedded high-performance mesh FTCE, a PSC was fabricated, with its cross-sectional FESEM images and schematic diagram presented in Fig. 5a. An aluminum-doped zinc oxide (AZO) layer of 50 nm thickness was deposited on the flat fine mesh electrode to enhance lateral conduction by filling mesh openings and protect the mesh from chemical damage by the halide ions contained in

the perovskite precursor solution. Ethylenediaminetetraacetic acid (EDTA)-complexed  $\text{SnO}_2$  (E- $\text{SnO}_2$ ) as an electron transport layer (ETL), a triple-cation perovskite layer  $[\text{Cs}_{0.05}(\text{FA}_{0.83}\text{MA}_{0.17})_{0.95}\text{Pb}(\text{I}_{0.88}\text{Br}_{0.12})_3]$ , and a 2,2',7,7'-tetrakis(N,N-di-p-methoxyphenylamine)-9,9-spirobifluorene (spiro-OMeTAD) layer as the hole transport layer (HTL) were sequentially deposited by spin coating, and finally, the top Au electrode was deposited by thermal evaporation. For comparison, a PSC was also fabricated on ITO film (Fig. S6). Figure 5b shows the current density–voltage ( $J$ – $V$ ) curves of the mesh-based and ITO-based devices, demonstrating that our mesh-based PSC exhibited a high PCE of 14.92%, an open-circuit voltage ( $V_{oc}$ ) of 1.09 V, a short-circuit current density ( $J_{sc}$ ) of  $18.49 \text{ mA cm}^{-2}$ , and a fill factor ( $FF$ ) of 74.20%. Our PSC demonstrated a performance comparable to that of the ITO-based PSC (Table 4 and Table S1). This excellent performance was attributed to the surface flatness of the fully-embedded-mesh FTCE, which prevented undesired current leakage and shunt currents. Moreover, the superior optoelectronic properties of our transparent electrode led to efficient electron transport in the device. To the best of our knowledge, the achieved PCE is the highest observed for metal mesh electrode-based PSCs.



**Fig. 4** a FESEM images and depth profiles, b sheet resistance distributions, and c transmittances of mesh patterns before and after the embedding process; d mechanical flexibility of embedded mesh

FTCE as measured by the change in resistivity after 100,000 cycles of bending at a curvature radius of 1 mm, e results of adhesion test for embedded-mesh FTCE

**Table 3** Comparison of flat mesh electrode performance

Materials in flat mesh electrodes	Line width [ $\mu\text{m}$ ]	Thickness [ $\mu\text{m}$ ]	$T$ [%]	$R_s$ [ $\Omega \text{sq}^{-1}$ ]	FoM ( $\sigma_{\text{dc}}/\sigma_{\text{opt}}$ )	References
Ag mesh	10	0.7	88.6	1.7	1777	This work
Ag mesh	4	2	94	0.6	9999	[34]
Ag mesh	10	2	80	0.5	3194	[35]
Ag mesh	4	2	89.7	2	1687	[26]
Ag mesh/Ag NW	5	2	86	1.5	1604	[36]
Ag/Ni mesh	2.4	3	88.6	2.1	1439	[27]
Ag mesh/PEDOT:PSS	3	2	80	1.2	1331	[37]
Ag mesh/PEDOT:PSS	32	1.3	90	4	871	[38]
Ag mesh/PEDOT:PSS	3	2	86	3	802	[28]
Ag mesh	3	2	87	5	523	[29]
Ag mesh	10	3.5	80.4	6.9	237	[30]
Ag mesh/Ag NW	10	—	87	13	201	[32]
Ag-Ni mesh	0.15	0.06	87.5	49.2	55	[39]



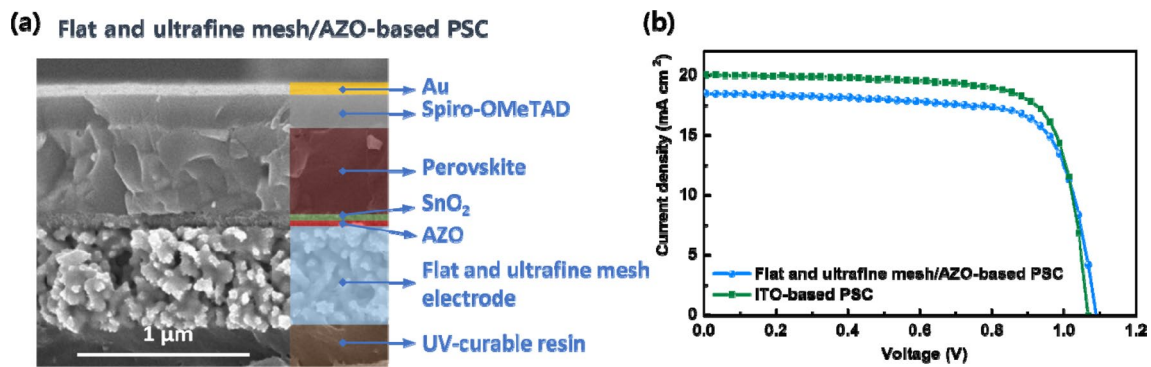


**Fig. 5** **a** Cross-sectional FESEM image of the PSC based on highly flat embedded-mesh electrode, **b**  $J$ - $V$  curves of PSCs based on ITO and embedded-mesh electrodes recorded under 1 sun illumination

**Table 4** Best-performing PSCs based on various metal mesh electrodes

Electrode type in PSC	$V_{oc}$ [V]	$J_{sc}$ [ $\text{mA cm}^{-2}$ ]	Fill factor [%]	PCE [%]	References
Embedded Ag mesh/AZO	1.09	18.49	74.20	14.92	This work
Embedded Ag mesh/PH1000	0.90	19.4	80	14.0	[28]
Embedded Ag mesh	0.70	16.80	64	7.53	[40]
Ag mesh/PH1000:ammonia:PEI	1.01	19.18	75	14.52	[41]
ITO/Ag mesh/AZO	1.00	20.95	66.1	13.86	[42]
Ni/Au mesh/PH1000	0.94	21.14	69.75	13.88	[43]

## 4 Conclusions

A manufacturable and scalable process was used to fabricate a highly flat, fully embedded fine mesh FTCE on a large area. Fine mesh patterns with various thicknesses were prepared by selective transfer printing and annealed by single-flash, double-flash, or multi-flash irradiation, and changes in electrical properties and sintering effectiveness were comprehensively investigated. Irradiation with a single flash of high-power light in a short time induced the rapid decomposition of residual insulating organics and NP sintering in the as-printed mesh. However, above a certain flash power threshold, the patterns were damaged because of a sudden large volume shrinkage. The use of two (or multiple) flashes allowed for a more stable and sufficient sintering without any damage to afford high conductivity ( $R_s = 1.7 \, \Omega \, \text{sq}^{-1}$ ). To embed these well-sintered mesh patterns, a PET film was laminated on patterns overlaid with UV-curable resin. The resin was then cured so that the mesh patterns became strongly coupled while remaining embedded in the cured resin. A completely flat mesh FTCE was obtained by peeling off the PET film with the cured resin and exhibited high optoelectronic performance ( $\text{FoM} = 1777$ ), outstanding mechanical flexibility ( $R/R_0 = 0.6\%$  after 100,000 bending cycles), and strong adhesion to the underlying substrate. Finally, this highly

flat, high-performance mesh FTCE was used to fabricate a PSC with a high PCE of 14.92% and was concluded to be suitable for emerging flexible optoelectronic applications.

**Acknowledgements** This work was supported by the National Research Foundation (NRF) of Korea funded by the Korean government (MSIP) (2019R1C1C1007931) and the Ministry of Trade, Industry & Energy (MOTIE, Korea) under the Industrial Technology Innovation Program (20000665). This study was also supported by the government-funded Research Program of the Korea Institute of Machinery and Materials Technology Innovation Program (NK224B) and the Korea Institute for Advancement of Technology (KIAT) through the Encouragement Program for the Industries of Economic Cooperation Region (Grant N0002310).

## References

1. Brown, T. M., De Rossi, F., Di Giacomo, F., Mincuzzi, G., Zardetto, V., Reale, A., et al. (2014). Progress in flexible dye solar cell materials, processes and devices. *Journal of Materials Chemistry A*, 2, 10788–10817.
2. Fan, X., Wang, J., Wang, H., Liu, X., & Wang, H. (2015). Bendable ITO-free organic solar cells with highly conductive and flexible PEDOT:PSS electrodes on plastic substrates. *ACS Applied Materials & Interfaces*, 7(30), 16287–16295.
3. Zou, J., Yip, H.-L., Hau, S. K., & Jen, A.K.-Y. (2010). Metal grid/conducting polymer hybrid transparent electrode for inverted polymer solar cells. *Applied Physics Letters*, 96, 203301.
4. Heo, J. H., Shin, D. H., Jang, M. H., Lee, M. L., Kang, M. G., & Im, S. H. (2017). Highly flexible, high-performance perovskite

- solar cells with adhesion promoted AuCl<sub>3</sub>-doped graphene electrodes. *Journal of Materials Chemistry A*, 5, 21146–21152.
5. Wang, T., Jing, L.-C., Zhu, Q., Ethiraj, A. S., Tian, Y., Zhao, H., et al. (2020). Fabrication of architectural structured polydopamine-functionalized reduced graphene oxide/carbon nanotube/PEDOT:PSS nanocomposites as flexible transparent electrodes for OLEDs. *Applied Surface Science*, 500, 143997.
  6. Han, J. W., Jung, B., Kim, D. W., Lim, K. T., Jeong, S.-Y., & Kim, Y. H. (2019). Transparent conductive hybrid thin-films based on copper-mesh/conductive polymer for ITO-free organic light-emitting diodes. *Organic Electronics*, 73, 13–17.
  7. Park, K., Woo, K., Kim, J., Lee, D., Ahn, Y., Song, D., et al. (2019). High-resolution and large-area patterning of highly conductive silver nanowire electrodes by reverse offset printing and intense pulsed light irradiation. *ACS Applied Materials & Interfaces*, 11(6), 14882–14891.
  8. Liu, Y., Shang, S., Mo, S., Wang, P., & Wang, H. (2020). Eco-friendly strategies for the material and fabrication of wearable sensors. *International Journal of Precision Engineering and Manufacturing-Green Technology*. <https://doi.org/10.1007/s40684-020-00285-5>.
  9. Ra, Y., La, M., Cho, S., Park, S. J., & Choi, D. (2020). Scalable batch fabrication of flexible, transparent and self-triggered tactile sensor array based on triboelectric effect. *International Journal of Precision Engineering and Manufacturing-Green Technology*. <https://doi.org/10.1007/s40684-020-00267-7>.
  10. Jeong, C., Joong, C., Lee, S., Feng, M. Q., & Park, Y.-B. (2020). Carbon nanocomposite based mechanical sensing and energy harvesting. *International Journal of Precision Engineering and Manufacturing-Green Technology*, 7, 247–267.
  11. Bazargan, A. M., Sharif, F., Mazinani, S., & Naderi, N. (2017). A high quality ITO/PET electrode for flexible and transparent optoelectronic devices. *Journal of Materials Science: Materials in Electronics*, 28, 2962–2969.
  12. Leterrier, Y., Médico, L., Demarco, F., Manson, J.-A.E., Betz, U., Escolà, M. F., et al. (2004). Mechanical integrity of transparent conductive oxide films for flexible polymer-based displays. *Thin Solid Films*, 460(1–2), 156–166.
  13. Li, T.-C., & Chang, R.-C. (2014). Improving the performance of ITO thin films by coating PEDOT:PSS. *International Journal of Precision Engineering and Manufacturing-Green Technology*, 1, 329–334.
  14. Kang, M., Kim, J., Jang, B., Chae, Y., Kim, J.-H., & Ahn, J.-H. (2017). Graphene-based three-dimensional capacitive touch sensor for wearable electronics. *ACS Nano*, 11(8), 7950–7957.
  15. Park, S., Vosguerichian, M., & Bao, Z. (2013). A review of fabrication and applications of carbon nanotube film-based flexible electronics. *Nanoscale*, 5, 1727–1752.
  16. Huseynova, G., Kim, Y. H., Lee, J.-H., & Lee, J. (2020). Rising advancements in the application of PEDOT:PSS as a prosperous transparent and flexible electrode material for solution-processed organic electronics. *Journal of Information Display*, 21(2), 71–91.
  17. Li, W., Zhang, H., Shi, S., Xu, J., Qin, X., He, Q., et al. (2020). Recent progress in silver nanowire networks for flexible organic electronics. *Journal of Materials Chemistry C*, 8, 4636–4674.
  18. Hwang, H., Kim, A., Zhong, Z., Kwon, H.-C., Jeong, S., & Moon, J. (2016). Reducible-shell-derived pure-copper-nanowire network and its application to transparent conducting electrodes. *Advanced Functional Materials*, 26(36), 6545–6554.
  19. Zhong, Z., Lee, H., Kang, D., Kwon, S., Choi, Y.-M., Kim, I., et al. (2016). Continuous patterning of copper nanowire-based transparent conducting electrodes for use in flexible electronic applications. *ACS Nano*, 10(8), 7847–7854.
  20. Kinner, L., Nau, S., Popovic, K., Sax, S., Burgués-Ceballos, I., Hermerschmidt, F., et al. (2017). Inkjet-printed embedded Ag-PEDOT:PSS electrodes with improved light out coupling effects for highly efficient ITO-free blue polymer light emitting diodes. *Applied Physics Letters*, 110, 101107.
  21. Zhong, Z., Ko, P., Seok, J. Y., Kim, H., Kwon, S., Youn, H., et al. (2020). Roll-to-roll reverse-offset printing combined with photonic sintering process for highly conductive ultrafine patterns. *Advanced Engineering Materials*. <https://doi.org/10.1002/adem.202000463>.
  22. Lee, H.-J., Cho, K.-Y., Oh, S., Park, S.-Y., Im, Y.-B., Yoon, Y.-J., et al. (2020). Optical and electrical properties of multilayer grid electrodes for highly durable transparent conductive electrodes. *International Journal of Precision Engineering and Manufacturing-Green Technology*. <https://doi.org/10.1007/s40684-020-00205-7>.
  23. Lee, S. H., Kim, S. W., Park, C. W., Jeong, H. E., OK, J. G., & Kwak, M. K. (2017). Scalable fabrication of flexible transparent heaters comprising continuously created metallic micromesh patterns incorporated with biomimetic anti-reflection layers. *International Journal of Precision Engineering and Manufacturing-Green Technology*, 4, 177–181.
  24. Jang, Y.-R., Joo, S.-J., Chu, J.-H., Uhm, H.-J., Park, J.-W., Ryu, C.-H., et al. (2020). A review on intense pulsed light sintering technologies for conductive electrodes in printed electronics. *International Journal of Precision Engineering and Manufacturing-Green Technology*. <https://doi.org/10.1007/s40684-020-00193-8>.
  25. Lee, H. B., Jin, W. Y., Ovhal, M. M., Kumar, N., & Kang, J.-W. (2019). Flexible transparent conducting electrodes based on metal meshes for organic optoelectronic device applications: a review. *Journal of Materials Chemistry C*, 7, 1087–1110.
  26. Xu, J.-L., Liu, Y.-H., Gao, X., Sun, Y., Shen, S., Cai, X., et al. (2017). Embedded Ag grid electrodes as current collector for ultraflexible transparent solid-state supercapacitor. *ACS Applied Materials & Interfaces*, 9(33), 27649–27656.
  27. Chen, X., Guo, W., Xie, L., Wei, C., Zhuang, J., Su, W., et al. (2017). Embedded Ag/Ni metal-mesh with low surface roughness as transparent conductive electrode for optoelectronic applications. *ACS Applied Materials & Interfaces*, 9(42), 37048–37054.
  28. Li, Y., Meng, L., Yang, Y. M., Xu, G., Hong, Z., Chen, Q., et al. (2016). High-efficiency robust perovskite solar cells on ultrathin flexible substrates. *Nature Communications*, 7, 10214.
  29. Zhou, L., Xiang, H.-Y., Shen, S., Li, Y.-Q., Chen, J.-D., Xie, H.-J., et al. (2014). High-performance flexible organic light-emitting diodes using embedded silver network transparent electrodes. *ACS Nano*, 8(12), 12796–12805.
  30. Yu, J.-S., Jung, G. H., Jo, J., Kim, J. S., Kim, J. W., Kwak, S.-W., et al. (2013). Transparent conductive film with printable embedded patterns for organic solar cells. *Solar Energy Materials & Solar Cells*, 109, 142–147.
  31. Cai, J., Zhang, M., Sun, Z., Zhang, C., Liang, C., Khan, A., et al. (2019). Highly-facile template-based selective electroless metallization of micro- and nanopatterns for plastic electronics and plasmonics. *Journal of Materials Chemistry C*, 7, 4363–4373.
  32. Jang, J., Im, H.-G., Jin, J., Lee, J., Lee, J.-Y., & Bae, B.-S. (2016). A flexible and robust transparent conducting electrode platform using an electroplated silver grid/surface-embedded silver nanowire hybrid structure. *ACS Applied Materials & Interfaces*, 8(40), 27035–27043.
  33. Liu, Y.-H., Xu, J.-L., Shen, S., Cai, X.-L., Chen, L.-S., & Wang, S.-D. (2017). High-performance, ultra-flexible and transparent embedded metallic mesh electrodes by selective electrodeposition for all-solid-state supercapacitor applications. *Journal of Materials Chemistry A*, 5, 9032–9041.
  34. Khan, A., Lee, S., Jang, T., Xiong, Z., Zhang, C., Tang, J., et al. (2016). High-performance flexible transparent electrode with an

- embedded metal mesh fabricated by cost-effective solution process. *Small (Weinheim an der Bergstrasse, Germany)*, 12(22), 3021–3030.
35. Lee, Y., Jin, W.-Y., Cho, K. Y., Kang, J.-W., & Kim, J. (2016). Thermal pressing of a metal-grid transparent electrode into a plastic substrate for flexible electronic devices. *Journal of Materials Chemistry C*, 4, 7577–7583.
  36. Oh, Y. S., Lee, H., Choi, D. Y., Lee, S.-U., Kim, H., Yoo, S., et al. (2016). High-performance, solution-processed, embedded multi-scale metallic transparent conductors. *ACS Applied Materials & Interfaces*, 8(17), 10937–10945.
  37. Mao, L., Chen, Q., Li, Y., Li, Y., Cai, J., Su, W., et al. (2014). Flexible silver grid/PEDOT:PSS hybrid electrodes for large area inverted polymer solar cells. *Nano Energy*, 10, 259–267.
  38. Jin, W.-Y., Ginting, R. T., Ko, K.-J., & Kang, J.-W. (2016). Ultra-smooth, fully solution-processed large-area transparent conducting electrodes for organic devices. *Scientific Reports*, 6, 36475.
  39. Kim, H.-J., Lee, S.-H., Lee, J., Lee, E.-S., Choi, J.-H., Jung, J.-H., et al. (2014). High-durable AgNi nanomesh film for a transparent conducting electrode. *Small (Weinheim an der Bergstrasse, Germany)*, 10(18), 3767–3774.
  40. Ou, Q.-D., Xie, H.-J., Chen, J.-D., Zhou, L., Li, Y.-Q., & Tang, J.-X. (2016). Enhanced light harvesting in flexible polymer solar cells: synergistic simulation of a plasmonic meta-mirror and a transparent silver mesowire electrode. *Journal of Materials Chemistry A*, 4, 18952–18962.
  41. Wang, J., Chen, X., Jiang, F., Luo, Q., Zhang, L., Tan, M., et al. (2018). Electrochemical corrosion of Ag electrode in the silver grid electrode-based flexible perovskite solar cells and the suppression method. *Solar RRL*, 2(9), 1800118.
  42. Zhang, W., Xiong, J., Wang, S., Liu, W.-E., Li, J., Wang, D., et al. (2017). Highly conductive and transparent silver grid/metal oxide hybrid electrodes for low-temperature planar perovskite solar cells. *Journal of Power Sources*, 337, 118–124.
  43. Chen, D., Fan, G., Zhang, H., Zhou, L., Zhu, W., Xi, H., et al. (2019). Efficient Ni/Au mesh transparent electrodes for ITO-free planar perovskite solar cells. *Nanomaterials*, 9, 932.
  44. Yang, H., Kwon, H.-C., Ma, S., Kim, K., Yun, S.-C., Jang, G., et al. (2020). Energy level-graded Al-doped ZnO protection layers for copper nanowire-based window electrodes for efficient flexible perovskite solar cells. *ACS Applied Materials & Interfaces*, 12, 13824–13835.

**Publisher's Note** Springer Nature remains neutral with regard to jurisdictional claims in published maps and institutional affiliations.



printing/coating techniques.



**Zhaoyang Zhong** is a Post Doctor at the Korea Institute of Machinery & Materials (KIMM), Daejeon, Korea. She received her MS degree from the Department of Electricity and Electronic Engineering at Gachon University in 2012 and received a PhD in 2018 from the Department of Materials Science and Engineering at Yonsei University. Her research interests focus mainly nanomaterial synthesis, light-assisted material processing and flexible device fabrication based on various

**Pyeongsam KO** is student researcher for MS degree of mechanical engineering at the Korea Institute of Machinery & Materials (KIMM) and Hanbat University, Daejeon, Korea. He received his BS in mechanical engineering from Hanbat University, Korea, in 2018. His research interests focus on flexible device fabrication based on various printing/coating techniques.

**Hongseok Youn** received MS and PhD degree in Department of Mechanical Engineering from Korea Advanced Institute of Science and Technology (KAIST) in 2005 and 2011 respectively. His research field was organic electronic devices (OLEDs/OPVs) and fabrication. From 2011 to 2014, he was a post-doc researcher in Department of Electrical Engineering and Computer Science, University of Michigan, Ann Arbor, USA. He joined Prof. Guo's laboratory and developed scalable and innovative optoelectronic device fabrication technique such as roll-to-roll coating and multi-film transfer. After completing post-doc research, he researched as a senior researcher at National Center for Center for Nano-Photonics Convergence Technology, Korea Institute of Industrial Technology (KITECH), Gwangju, South Korea in 2014. Now he is associate professor in Department of Mechanical Engineering from

Hanbat National University, Daejeon, South Korea since he has been joined as assistant professor from 2015..



**Areum Kim** is a senior researcher at the Korea Institute of Machinery & Materials (KIMM), Daejeon, Korea. She received her BS in 2010 and a PhD in 2016 from the Department of Materials Science and Engineering at Yonsei University. She joined in corporate R&D center at LG chem as a senior researcher from 2016 to 2019. Her research interests focus mainly on fabrication of energy conversion and storage devices based on solution process.



printing/coating techniques.

**Kyoohee Woo** is a senior researcher at the Korea Institute of Machinery & Materials (KIMM), Daejeon, Korea. He received his BS in 2007 and a PhD in 2013 from the Department of Materials Science and Engineering at Yonsei University. He joined material R&D team at LG display as a senior research engineer from 2013 to 2014. His research interests focus mainly on nanomaterial synthesis, light-assisted material processing and flexible device fabrication based on various